INTERNATIONAL JOURNAL FOR NUMERICAL METHODS IN FLUIDS, VOL. 11, 907–934 (1990)

FINITE DIFFERENCE AND FINITE ELEMENT METHODS FOR MHD CHANNEL FLOWS

J. I. RAMOS

Department of Mechanical Engineering, Carnegie-Mellon University, Pittsburgh, PA 15213, U.S.A.

AND

N. S. WINOWICH

Department of Mechanical Engineering, University of Maine, Orono, ME 04469, U.S.A.

SUMMARY

A Galerkin finite element method and two finite difference techniques of the control volume variety have been used to study magnetohydrodynamic channel flows as a function of the Reynolds number, interaction parameter, electrode length and wall conductivity. The finite element and finite difference formulations use unequally spaced grids to accurately resolve the flow field near the channel wall and electrode edges where steep flow gradients are expected. It is shown that the axial velocity profiles are distorted into M-shapes by the applied electromagnetic field and that the distortion increases as the Reynolds number, interaction parameter and electrode length are increased. It is also shown that the finite element method predicts larger electromagnetic pinch effects at the electrode entrance and exit and larger pressure rises along the electrodes than the primitive-variable and streamfunction–vorticity finite difference formulations. However, the primitive-variable formulation predicts steeper axial velocity gradients at the channel walls and lower axial velocities at the channel centreline than the streamfunction–vorticity finite difference and the finite element methods. The differences between the results of the finite difference and finite element methods are attributed to the different grids used in the calculations and to the methods used to evaluate the pressure field. In particular, the computation of the velocity field from the streamfunction–vorticity formulation introduces computational noise, which is somewhat smoothed out when the pressure field is calculated by integrating the Navier–Stokes equations. It is also shown that the wall electric potential increases as the wall conductivity increases and that, at sufficiently high interaction parameters, recirculation zones may be created at the channel centreline, whereas the flow near the wall may show jet-like characteristics.

KEY WORDS Finite Elements Magnetohydrodynamics Finite Differences Primitive Variables

INTRODUCTION

The objective of this paper is twofold. First, an analysis of magnetohydrodynamic (MHD) channel flows, which have practical applications as direct current (DC) electromagnetic pumps for liquid metal fast breeder reactors and in lithium blankets of conceptual fusion reactors, is presented. The analysis involves the determination of both the electric and hydrodynamic fields in the channel as a function of the Reynolds number, interaction parameter, electrode length and wall conductivity.

The second objective of the paper is to present a detailed comparison of the electric and hydrodynamic fields calculated by means of three numerical techniques: a primitive-variable finite element formulation, a streamfunction–vorticity finite difference method and a primitive-variable finite difference scheme of the control volume variety.

0271–2091/90/140907–28$14.00 *Received July 1989*

Previous numerical calculations of MHD channel flows include those of References 1–10. Wu[1] studied unsteady, fully developed MHD flows by means of a finite element method. Singh and Lal[2,3] analysed fully developed MHD flows and determined the effects of the applied magnetic field orientation and wall conductivity on both the electric and hydrodynamic fields. Gel'fgat *et al.*[4] used a streamfunction–vorticity finite difference formulation to analyse MHD channel flows with non-uniform magnetic fields and non-conducting walls at low Reynolds and Hartmann numbers.

Yagàwa and Masuda[5] used an incremental finite element technique to study MHD channel flows at high magnetic Reynolds numbers in which the induced magnetic field cannot be neglected. They also analysed a lithium blanket at high interaction parameter and neglected the convection and viscous terms in the momentum (Navier–Stokes) equations, i.e. the Lorentz body force was balanced by the pressure gradient.

Most of these studies employed an applied magnetic field parallel to the flow and neglected the inertia (or convection) terms in the fluid equations. By way of contrast, the formulation and results presented in this paper are for finite Reynolds number flows where the inertia terms cannot be neglected. Furthermore, this study considers MHD channel flows where the applied magnetic field is perpendicular to the flow direction.

The first numerical calculations relevant to the geometry and parameters considered in this paper were performed by Winowich and Hughes,[6] who used a primitive-variable finite element formulation. Their preliminary calculations for a non-conducting wall electromagnetic pump indicated that the non-uniform applied magnetic field produces M-shaped axial velocity profiles in the fluid.

Ramos and Winowich[7] used a time-dependent primitive-variable finite difference method to analyse an electromagnetic pump with non-conducting walls and showed that the upstream and downstream boundaries of the computational domain must be located sufficiently far away from the electrodes in order for the flow to be fully developed at those boundaries. Ramos and Winowich[7] also showed that the locations of the upstream and downstream boundaries are functions of the Reynolds number and interaction parameter and that the axial velocity profiles are distorted into M-shapes as a consequence of the applied magnetic field.

Winowich *et al.*[8] used a primitive-variable finite element formulation to analyse MHD channel flows as a function of the electrode length and wall conductivity and showed that the channel wall electric potential increases as the wall conductivity increases. Winowich *et al.*[8] also compared their numerical results with those of Ramos and Winowich[7] for an unrealistic (non-dimensional) electrode length equal to unity and claimed that the differences between the results of the finite element and finite difference methods were due to the different meshes employed in the calculations.

Winowich[9] used a primitive-variable finite element formulation to analyse MHD channel flows and determined the effects of the Reynolds number, interaction parameter, electrode length and wall conductivity on the electric and hydrodynamic fields. Winowich and Ramos[10] compared some of the finite element results of Winowich[9] with those obtained by means of a streamfunction–vorticity finite difference method and a primitive-variable finite difference technique of the control volume variety. The results of such a comparison indicated that the finite element method predicts a higher electromagnetic pinch effect at the electrode entrance and exit, and higher pressure than the primitive-variable and streamfunction–vorticity finite difference formulations. However, the primitive-variable finite difference formulation predicted steeper axial velocity gradients at the channel wall and more pronounced M-shaped axial velocity profiles than the streamfunction–vorticity and finite element methods. The differences between the results of the finite element and finite difference techniques were attributed to the different meshes used in the

calculations. These differences may also be related to the numerical methods used to evaluate the pressure field. In particular, the finite element method used bilinear and biquadratic interpolation functions for the pressure and velocity fields respectively, whereas donor cell/central difference formulae were used to calculate the spatial derivatives in the finite difference formulations.

In addition to the numerical studies briefly discussed in previous paragraphs, numerous theoretical (asymptotic) analyses of MHD channel flows have appeared in the literature. Hunt[11] and Hunt and Stewartson[12] studied MHD flows in rectangular ducts with uniform transverse magnetic fields and obtained asymptotic solutions for perfectly conducting walls perpendicular to the applied magnetic field and thin walls of arbitrary conductivity parallel to the applied magnetic field. Hunt and Leibovich[13] used asymptotic methods to study variable-area converging and diverging MHD channel flows at high interaction parameters and showed that the velocity profiles are very sensitive to the variation of the duct width with axial distance.

MHD flows at high Hartmann numbers and interaction parameters have been studied in References 14–19. At high interaction parameters the inertia terms in the Navier–Stokes equations are negligible compared with the electromagnetic body forces, and the flow field can be divided into a core region and velocity layers parallel and normal (Hartmann's layers) to the applied magnetic field. In the core region the convective and viscous terms are negligible and the pressure gradient balances the electromagnetic body forces.[14] The velocity layers parallel to the applied magnetic field may be either secondary boundary layers adjacent to the walls or free shear layers. In the secondary layers the flow is characterized by high velocities induced by the channel geometry and the non-uniform magnetic field.

Hunt and Ludford,[15] Walker *et al.*[16, 17] and Walker and Ludford[18] studied MHD flows in constant- and variable-area rectangular channels with all the walls either insulated or conducting, by means of asymptotic methods, and showed that thin, high-velocity boundary layers are formed in a diverging channel; these boundary layers carry almost the entire flow. Holroyd and Walker[19] considered steady MHD flows with non-uniform applied magnetic fields and wall conductivity in pipes of circular cross-section at high Hartmann numbers and interaction parameters, and showed that a pair of eddies is formed near the pipe centreline where the applied magnetic field is weakest. These eddies induce flow reversals with associated large pressure drops.

In this paper a primitive-variable finite element method, a streamfunction–vorticity finite difference technique and a primitive-variable finite difference formulation of the control volume variety are used to determine the electric and hydrodynamic fields in an MHD channel flow with an applied magnetic field perpendicular to the flow direction, as a function of the Reynolds number, interaction parameter, wall conductivity and electrode length.

The calculations presented in this paper are valid for low interaction parameters and moderate Reynolds numbers, and the inertia and viscous terms in the Navier–Stokes equations cannot be neglected. These calculations show that the axial velocity profiles develop peaks near the wall; the magnitude of these velocity peaks increases as the interaction parameter is increased and, for sufficiently large values of the interaction parameter, flow reversals may appear at the channel centreline in qualitative agreement with the asymptotic analyses of References 14–19.

PROBLEM FORMULATION

Consider the DC electromagnetic pump shown schematically in Figure 1. The pump consists of a duct, two electrodes and two magnetic pole pieces.

The hydrodynamic and electromagnetic fields in Figure 1 are three-dimensional, and the electromagnetic pump will be idealized as the two-dimensional magnetohydrodynamic (MHD) channel flow shown schematically in Figure 2. We will assume that the flow is steady,

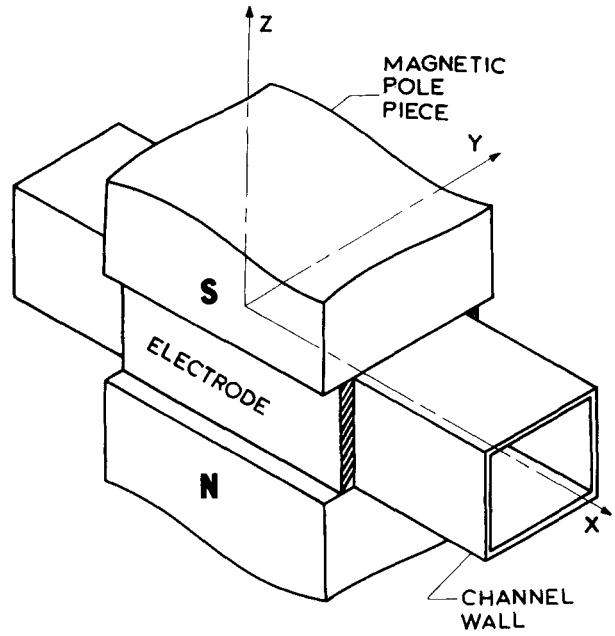

Figure 1. Schematic of a DC electromagnetic pump

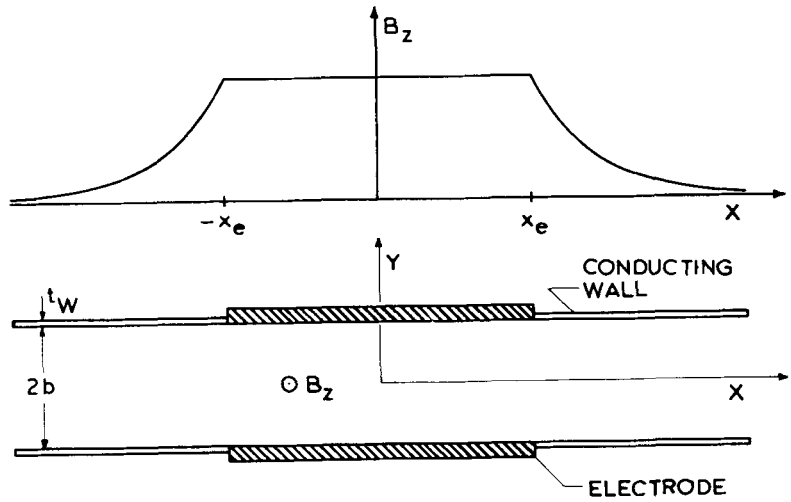

Figure 2. Schematic of a two-dimensional MHD channel flow configuration and applied magnetic field

incompressible, laminar, isothermal, Newtonian and electrically conducting and that the electrodes are perfect conductors, while the channel wall extensions may have finite electrical conductivity.

In Figure 2, B_z denotes the applied magnetic field, x and y are the co-ordinates along and transverse to the channel axis respectively, $2b$ is the channel width, t_w is the wall thickness and $L_e = 2x_e$ denotes the electrode length, i.e. $-x_e$ and x_e correspond to the electrode entrance and exit respectively.

Under the assumptions stated above, the hydrodynamic flow field is governed by the equations

$$\frac{\partial u}{\partial x}+\frac{\partial v}{\partial y}=0, \tag{1}$$

$$\rho\left(u\frac{\partial u}{\partial x}+v\frac{\partial u}{\partial y}\right)=-\frac{\partial p}{\partial x}+\mu\left(\frac{\partial^2 u}{\partial x^2}+\frac{\partial^2 u}{\partial y^2}\right)+f_x, \tag{2}$$

$$\rho\left(u\frac{\partial v}{\partial x}+v\frac{\partial v}{\partial y}\right)=-\frac{\partial p}{\partial y}+\mu\left(\frac{\partial^2 v}{\partial x^2}+\frac{\partial^2 v}{\partial y^2}\right)+f_y, \tag{3}$$

where u and v are the axial and transverse velocity components respectively, ρ (=constant) is the fluid density, p is the pressure, μ (=constant) is the dynamic viscosity of the fluid and f_x and f_y denote the components of the body forces per unit volume in the x- and y-direction respectively.

Introducing the non-dimensional variables

$$x^*=x/b, \qquad y^*=y/b, \qquad u^*=u/u_m, \qquad v^*=v/u_m, \qquad p^*=p/\rho u_m^2 \tag{4}$$

into equations (1)–(3), the following system results:

$$\frac{\partial u^*}{\partial x^*}+\frac{\partial v^*}{\partial y^*}=0, \tag{5}$$

$$u^*\frac{\partial u^*}{\partial x^*}+v^*\frac{\partial u^*}{\partial y^*}=-\frac{\partial p^*}{\partial x^*}+\frac{1}{Re}\left(\frac{\partial^2 u^*}{\partial x^{*2}}+\frac{\partial^2 u^*}{\partial y^{*2}}\right)+F_{x^*}^*, \tag{6}$$

$$u^*\frac{\partial v^*}{\partial x^*}+v^*\frac{\partial v^*}{\partial y^*}=-\frac{\partial p^*}{\partial y^*}+\frac{1}{Re}\left(\frac{\partial^2 v^*}{\partial x^{*2}}+\frac{\partial^2 v^*}{\partial y^{*2}}\right)+F_{y^*}^*, \tag{7}$$

where u_m is the mass-averaged velocity, $Re=\rho b u_m/\mu$ is the Reynolds number based on the channel half-width and the mass-averaged velocity, and

$$F_{x^*}^*=f_x b/\rho u_m^2, \qquad F_{y^*}^*=f_y b/\rho u_m^2. \tag{8}$$

The body forces f_x and f_y in equations (2) and (3) can be determined from Maxwell's equations, which can be written as

$$\nabla\cdot\mathbf{D}=\rho_e, \tag{9}$$

$$\nabla\cdot\mathbf{B}=0, \tag{10}$$

$$\nabla\times\mathbf{H}=\partial\mathbf{D}/\partial t+\mathbf{J}, \tag{11}$$

$$\nabla\times\mathbf{E}=-\partial\mathbf{B}/\partial t, \tag{12}$$

where ρ_e is the electric charge density, $\mathbf{D}$ is the electric displacement, $\mathbf{B}$ is the magnetic flux density, $\mathbf{H}$ is the magnetic field intensity, t is time, $\mathbf{E}$ is the electric field intensity and $\mathbf{J}$ is the electric current density.

For a time-independent magnetic field, equation (12) states that the electric field is irrotational, i.e.

$$\mathbf{E}=-\nabla\phi, \tag{13}$$

where ϕ is the electric potential.

Equation (13) can be written in non-dimensional form as

$$\mathbf{E}^*=-\nabla^*\phi^*=-\left(\frac{\partial\phi^*}{\partial x^*}\mathbf{i}+\frac{\partial\phi^*}{\partial \mathbf{y}^*}\mathbf{j}\right), \tag{14}$$

where

$$\mathbf{E}^* = \mathbf{E}/B_0 u_m, \qquad \phi^* = \phi/b u_m B_0, \tag{15}$$

i and **j** are the unit vectors in the x- and y-direction respectively and B_0 is a characteristic value of the applied magnetic field.

The applied magnetic field **B** is assumed to act in the z-direction only, i.e. $\mathbf{B} = (0, 0, B_z)$, and has constant magnitude between the electrodes; beyond the electrodes the applied magnetic field decays exponentially to zero, i.e.

$$B_z(x) = B_0, \quad |x| \leqslant x_e, \tag{16}$$

$$B_z(x) = B_0 \exp[-\xi(|x| - x_e)/b], \quad |x| \geqslant x_e, \tag{17}$$

where $\xi\,(=1)$ denotes the magnetic field spatial decay. The applied magnetic field shown in Figure 2 is solenoidal but not irrotational. The violation of the irrotationality condition is the result of reducing the three-dimensional problem shown in Figure 1 to the two-dimensional one presented in Figure 2.

Equations (16) and (17) can be written in the non-dimensional form

$$B_z^* = 1, \quad |x^*| \leqslant x_e^*, \tag{18}$$

$$B_z^* = \exp[-\xi(|x^*| - x_e^*)], \quad |x^*| > x_e^*, \tag{19}$$

where $B_z^* = B_z/B_0$.

The current density **J** is related to **E**, $\mathbf{v} = (u, v)$ and **B** through Ohm's law for isotropic moving media, i.e.

$$\mathbf{J} = \sigma_f(\mathbf{E} + \mathbf{v} \times \mathbf{B}), \tag{20}$$

where σ_f is the fluid electric conductivity.

Equation (20) can be written in the non-dimensional form

$$\mathbf{J}^* = R_m(\mathbf{E}^* + \mathbf{v}^* \times \mathbf{B}^*), \tag{21}$$

where $\mathbf{J}^* = \mathbf{J}/(B_0/b\mu_0)$, $R_m = \mu_0 \sigma_f u_m b$ is the magnetic Reynolds number and μ_0 is the permeability of free space.

The body force $\mathbf{f} = (f_x, f_y, 0)$ in equations (2) and (3) is the electromagnetic Lorentz force given by

$$\mathbf{f} = \mathbf{J} \times \mathbf{B} = \sigma_f(\mathbf{E} + \mathbf{v} \times \mathbf{B}) \times \mathbf{B}. \tag{22}$$

Equation (22) can be written in non-dimensional form as

$$\mathbf{F}^* = A(\mathbf{J}^* \times \mathbf{B}^*) = N(-\nabla^* \phi^* + \mathbf{v}^* \times \mathbf{B}^*) \times \mathbf{B}^*, \tag{23}$$

where $A = B_0^2/\mu_0 \rho u_m^2$ is the Alfven number and $N = \sigma_f B_0^2 b/\rho u_m$ is the interaction parameter.

For the applied magnetic field shown in Figure 2, the electromagnetic body forces in equations (6) and (7) are given by

$$F_{x^*}^* = -NB_z^*(\partial\phi^*/\partial y^*) - NB_z^{*2} u^*, \tag{24}$$

$$F_{y^*}^* = NB_z^*(\partial\phi^*/\partial x^*) - NB_z^{*2} v^*. \tag{25}$$

The electric current density vector **J** (or **J***) is solenoidal, i.e.

$$\nabla \cdot \mathbf{J} = 0 \quad \text{or} \quad \nabla^* \cdot \mathbf{J}^* = 0. \tag{26}$$

Therefore, using equations (14) and (21), equation (26) can be written as

$$\nabla^2 \phi = \nabla \cdot (\mathbf{v} \times \mathbf{B}) \quad \text{or} \quad \nabla^{*2} \phi^* = \nabla^* \cdot (\mathbf{v}^* \times \mathbf{B}^*). \tag{27}$$

The solution of equation (27) yields the electric potential ϕ^*, which can be substituted into equation (14) to obtain the electric field intensity vector $\mathbf{E}^*$. Once ϕ^* is known, the electromagnetic forces (see equations (24) and (25)) can be calculated and then substituted into equations (5)–(7) to determine the hydrodynamic field. Note that equations (5)–(7), (24), (25) and (27) are nonlinearly coupled through the velocity vector $\mathbf{v}^* = (u^*, v^*)$ and the electric potential ϕ^*. Note also that the equations (5)–(7) are invariant under translations in pressure.

BOUNDARY CONDITIONS

Equations (1)–(3) and (27) are subject to the boundary conditions

$$u(-\infty, y) = u(\infty, y) = 1{\cdot}5u_0[1-(y/b)^2], \tag{28}$$

$$v(-\infty, y) = v(\infty, y) = 0, \tag{29}$$

$$p(-\infty, y) = 0, \tag{30}$$

$$u(x, b) = v(x, b) = 0 \tag{31}$$

$$\partial u(x, 0)/\partial y = 0, \qquad v(x, 0) = 0, \tag{32}$$

$$\phi(x, 0) = \phi(-\infty, y) = \phi(\infty, y) = 0, \tag{33}$$

$$\phi(x, b) = \phi_e, \quad |x| \leqslant x_e, \tag{34}$$

where $1{\cdot}5\,u_0$ denotes the axial velocity at the channel centreline far upstream from the applied electric and magnetic fields, and ϕ_e is the electrode potential.

The boundary conditions at the wall for $|x^*| > x_e$ depend on the wall electrical characteristics. For a non-electrically conducting wall

$$\partial\phi(x, b)/\partial y = 0, \quad |x| > x_e, \tag{35}$$

whereas for an electrically conducting wall the boundary conditions for the electric potential can be determined as follows. If the wall thickness t_w is much smaller than the electrode spacing, i.e. $t_w \ll b$, the electric potential at the wall, ϕ_w, will mainly be a function of the axial co-ordinate, i.e. $\phi_w = \phi_w(x)$, and a current balance on a small segment Δx of the wall will relate the axial current density in the wall, J_w, to the transverse current density in the fluid evaluated at the wall, i.e.

$$t_w(\mathrm{d}J_w/\mathrm{d}x) = J_y(x, b), \qquad |x| > x_e. \tag{36}$$

Furthermore, applying Ohm's law at the wall yields

$$-t_w\sigma_w(\partial^2\phi_w/\partial x^2) = J_y(x, b), \quad |x| > x_e, \tag{37}$$

where $\phi_w(x)$ is the wall electric potential, σ_w is the electrical conductivity of the wall and

$$\phi_w(-\infty) = \phi_w(\infty) = 0. \tag{38}$$

Equations (28) and (29) indicate that far upstream and far downstream of the electrodes the velocity profiles correspond to that of a fully developed, laminar channel flow; equation (30) fixes the upstream pressure (note that the incompressible Navier–Stokes equations are invariant under translations in pressure); equation (31) corresponds to the no-slip condition at the channel wall; equation (32) is the condition of symmetry at the channel centreline; equation (33) indicates that the electric potential is zero far upstream and far downstream of the electrodes and at the channel centreline; equation (34) corresponds to the electrode potential (note that the electrodes were assumed to be perfect conductors).

The mass-averaged velocity through the channel is u_0, i.e. $u_m = u_0$, and equations (28)–(38) can be written in the non-dimensional form

$$u^*(-\infty, y^*) = u^*(\infty, y^*) = 1{\cdot}5(1 - y^{*2}), \tag{39}$$

$$v^*(-\infty, y^*) = v^*(\infty, y^*) = 0, \tag{40}$$

$$p^*(-\infty, y^*) = 0, \tag{41}$$

$$v^*(x^*, 0) = \partial u^*(x^*, 0)/\partial y^* = 0, \tag{42}$$

$$\phi^*(x^*, 0) = \phi^*(-\infty, y^*) = \phi^*(\infty, y^*) = 0, \tag{43}$$

$$\phi^*(x^*, 1) = \phi_c^* = \phi_e/bu_m B_0, \quad |x^*| \leqslant x_c^* = L_c^*/2 = x_e/b = L_e/2b, \tag{44}$$

$$\partial\phi^*(x^*, 1)/\partial y^* = 0, \quad |x^*| > L_e/2b \quad \text{(non-conducting wall)}, \tag{45}$$

$$-R_m \bar{\sigma} \partial^2 \phi_w^*/\partial x^{*2} = J_{y^*}^*(x^*, 1), \quad |x^*| > L_e/2b \quad \text{(conducting wall)}, \tag{46}$$

$$\phi_w^*(-\infty) = \phi_w^*(\infty) = 0 \quad \text{(conducting wall)}, \tag{47}$$

where $\phi_w^* = \phi_w/bu_m B_0$ is the non-dimensional electric potential of the wall, $\mathbf{J}^* = (J_{x^*}^*, J_{y^*}^*)$ and $\bar{\sigma} = \sigma_w t_w/\sigma_f b$ is the wall conductivity parameter, which is the ratio of the wall conductance to the fluid conductance.

For the sake of convenience we will drop all the stars in the non-dimensional equations in the next sections, with the understanding that hereon all the variables are dimensionless.

NUMERICAL METHODS

Equations (5)–(7), (27) and (46) for conducting walls were solved by means of a finite element method and two finite difference techniques subject to the boundary conditions given by equations (39)–(44), (45) for non-conducting walls and (46), (47) for conducting walls. The infinite domain $-\infty < x < \infty$ was truncated to a finite one, and the locations of the upstream and downstream boundaries of the computational domain were determined so as to minimize the influence of their location on the computed hydrodynamic and electric fields. The length of the computational domain and the number of grid points and finite elements are given in the next subsections, where the finite element and finite difference methods used to solve equations (5)–(7), (27) and (46) for conducting walls are presented.

Galerkin finite element method

A Galerkin finite element method was used to solve equations (5)–(7), (27) and (46), and the flow domain was subdivided into rectangular elements for the fluid (Figure 3) and one-dimensional line elements for the conducting wall, i.e. for equation (46). The primitive variables over a given finite element E were approximated as

$$u_E \approx \hat{u}_E = \sum_E \Phi_m u_m, \qquad v_E \approx \hat{v}_E = \sum_E \Phi_m v_m, \tag{48}$$

$$p_E \approx \hat{p}_E = \sum_E \psi_n p_n, \qquad \phi_E \approx \hat{\phi}_E = \sum_E \Phi_m \phi_m, \tag{49}$$

where u_m, v_m, p_n and ϕ_m are the nodal amplitudes (unknowns), $\psi_m(x, y)$ and $\Phi_m(x, y)$ are bilinear and biquadratic interpolation functions respectively and the summation symbol refers to the nodes of the element E.

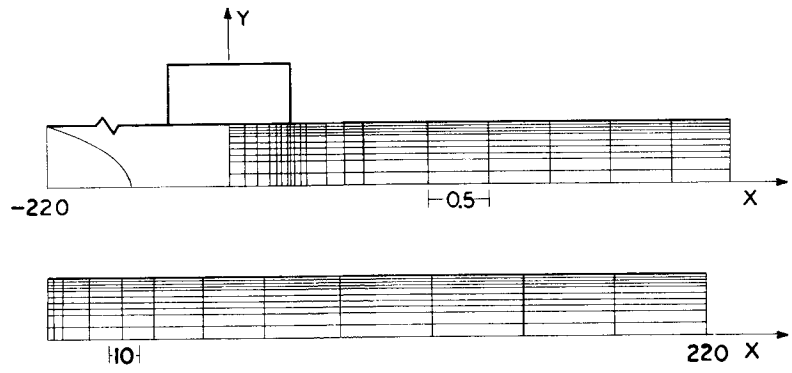

Figure. 3. Schematic of the finite element grid

A Galerkin finite element method was used to derive the discrete form of the governing equations for each element, which, when assembled over the computational domain, result in the following system of algebraic equations:

$$\mathbf{A}\{X\} = \{F\}, \qquad \mathbf{L}\{\phi\} = \{G\} \tag{50a,b}$$

where $\{X\}$ is the vector of the velocity–pressure nodal amplitudes, **A** and **L** are global coefficient matrices, $\{\phi\}$ represents the nodal amplitudes of the electric potential, $\{F\}$ denotes the assembled right-hand sides of the continuity and Navier–Stokes equations and $\{G\}$ is the assembled right-hand-side vector of the fluid and wall electric potentials.

The Newton–Raphson method was used to solve the non-linear equation (50a), and a frontal solver[20] was used to calculate the vectors $\{X\}$ and $\{\phi\}$. Since the velocity–pressure equations (equation (50a)) and the electric potential equations (equation (50b)) are coupled through their right-hand-side terms (see equations (24), (25) and (27)), the solution of equations (50) was obtained by means of an iterative technique as follows. The electromagnetic forces were guessed and equation (50a) was solved to determine the nodal amplitudes of the velocity and pressure fields. The velocity field was then used to evaluate the vector $\{G\}$ in equation (50b), whose solution gives the nodal amplitudes of the electric potential. The electric potential thus obtained was then used to solve equation (50a) and this iterative process was repeated until a specified convergence criterion was satisfied.

The iterative technique described in the previous paragraph is such that the solutions of the velocity and pressure fields, and that of the electric potential, are decoupled within each iteration.

A more efficient technique would have been to write the coupled equations for $\{X\}$ and $\{\phi\}$ as

$$\mathbf{B}\{\Psi\} = \{R\}, \tag{51}$$

where $\{\Psi\}$ denotes the nodal amplitudes of the velocity, pressure and electric potential, **B** is a global coefficient matrix and $\{R\}$ denotes the corresponding right-hand-side vector.

Equation (51) could be solved by means of a Newton–Raphson method with a frontal solver, and its solution provides the nodal amplitude vector. However, the dimensions of the matrix **B** are much larger than those of the matrices **A** and **L**, and equation (51) was not used owing to the size of the computer (CDC 815) used to solve the finite element equations.

In order to accelerate the convergence of the finite element method, an incremental technique based on the interaction parameter, which appears in the electromagnetic body forces (see equations (24) and (25)), was used.

A schematic of the finite element mesh is shown in Figure 3. This mesh is symmetric with respect to the y-axis, and the hydrodynamic and electric fields need to be calculated in $0 \leqslant y \leqslant 1$.

The flow field upstream and downstream of the electrodes is not symmetric, even though the channel geometry, electrodes and applied magnetic field are symmetric with respect to the y-axis, In order to ensure that the flow field far upstream and far downstream of the electrodes corresponds to a fully developed laminar condition for the range of parameters analysed in this paper, the $-\infty < x < \infty$ was truncated to $-220 \leqslant x \leqslant 220$, where x is the non-dimensional axial co-ordinate.

The finite element mesh shown in Figure 3 concentrates the finite elements near the channel wall and at the electrode entrance and exit where steep gradients are expected. The size of the elements increases from $x = x_e$ to $x = 220$ and from $x = -x_e$ to $x = -220$. Note that the axial length of the computational domain is 440 whereas the non-dimensional channel half-width is unity, i.e. the finite elements have large aspect ratios, particularly near the upstream and downstream boundaries of the computational domain.

Primitive-variable finite difference formulation

Equations (5)–(7), (27) and (46) for conducting walls were also solved by means of a finite difference technique which uses a primitive-variable formulation. The finite difference method is of the control volume variety and uses a staggered grid where the scalar variables, i.e. p, ϕ and ϕ_w, are stored at the grid points, whereas the velocity components u and v are stored at the midpoints in order to accurately calculate the convective fluxes at the computational cell boundaries.

The number and location of the grid points used in the primitive-variable finite difference method were selected by trial and error in order to ensure that the electric and hydrodynamic fields are grid-independent, and upwind/central difference approximations were used to evaluate the convective fluxes at the cell boundaries. A 256×64 mesh resulted in grid-independent results for calculations performed with $Re = 1000$, $N = 10$, $\bar{\sigma} = 0{\cdot}3$, $L_e = 1$ and $\phi_e = 1{\cdot}5$, and this grid was also used at the lower Reynolds numbers and interaction parameters discussed in the section on the presentation of results.

The pressure was calculated by means of the SIMPLE algorithm[21] in order to satisfy the continuity equation, and the finite difference equations of u, v, p, ϕ and ϕ_w were solved iteratively using a line Gauss–Seidel method starting at the upstream boundary and sweeping the computational domain axially as many times as required to obtain convergence for each dependent variable.[22] This sweeping procedure was used for all the dependent variables until a specified convergence criterion was satisfied.

The finite difference grid was concentrated at the channel wall and at the electrode entrance and exit where large gradients are expected. The grid was symmetric with respect to the y-axis, even though the hydrodynamic and electric fields are not symmetric with respect to that axis. A geometric progression was used to calculate the location of the grid points in the axial direction in $0 \leqslant x \leqslant x_e$, and an exponential function was employed to distribute the grid points axially for $x \geqslant x_e$. The number of grid points in the electrode region as well as the geometric progression ratio and the exponential function were selected so as to ensure that the results are grid-independent.

Streamfunction–vorticity finite difference formulation

Equations (5)–(7), (27) and (46) for conducting walls were also solved in the same grid as that discussed in the previous section using a streamfunction–vorticity formulation. The formulation takes advantage of the fact that for a two-dimensional incompressible flow there exists a non-

dimensional streamfunction ξ such that

$$u = \partial\xi/\partial y, \qquad v = -\partial\xi/\partial x, \tag{52}$$

where all the variables used in this and the next sections are dimensionless.

Equation (52) automatically satisfies the continuity equation (5) if ξ is a continuous function with continuous derivatives up to the second order.

In a two-dimensional flow the vorticity $\omega = \nabla \times \mathbf{v}$ is in the direction of the z-axis and can be written as $\boldsymbol{\omega} = (0, 0, \omega)$ where

$$\omega = \frac{\partial v}{\partial x} - \frac{\partial u}{\partial y}. \tag{53}$$

Substitution of equation (52) into equation (53) yields

$$\nabla^2 \xi = -\omega, \tag{54}$$

and taking the curl of equations (6) and (7) yields

$$u\frac{\partial \omega}{\partial x} + v\frac{\partial \omega}{\partial y} = \frac{1}{Re}\nabla^2\omega + \frac{\partial F_y}{\partial x} - \frac{\partial F_x}{\partial y}. \tag{55}$$

Equations (27), (46), (54) and (55) were solved for ϕ, ϕ_w, ξ and ω using upwind/central differences for the convection terms in an iterative manner. A line Gauss–Seidel method, similar to that described in the previous section, was used to solve equations (54) and (55) until a specified convergence criterion for each dependent variable was reached. The boundary conditions for ξ and ω are

$$\xi(x, 0) = 0, \qquad \omega(x, 0) = 0, \qquad \xi(x, 1) = 1, \tag{56}$$

and the vorticity at the wall was evaluated by means of a first-order accurate finite difference formula.[23]

Equations (54) and (55) involve two dependent variables, ξ and ω, and their solution is more computationally efficient than that of equations (5)–(7), which involve three dependent variables. However, the velocity field is obtained from the streamfunction–vorticity formulation by differentiation of the streamfunction; this differentiation introduces computational noise because ξ is only calculated at discrete grid points. Furthermore, the pressure field must be determined from the integration of equations (6) and (7) subject to equation (41) and $\partial p(x, 0)/\partial y = 0$. Since the integration of equations (6) and (7) is a smoothing operation, the pressure field determined from the integration of equations (6) and (7) is not as 'noisy' as those of u and v.

The solution of equations (54) and (55) was obtained in the same grid as that of the primitive-variable finite difference formulation described in the previous section using a staggered grid. Furthermore, the term $\partial\omega/\partial t$ was added to the left-hand side of equation (55) in order to increase the diagonal terms of the discretized form of equation (55) and accelerate the convergence rate. The pseudo-time derivative was discretized as

$$\frac{\partial \omega}{\partial t} \approx \frac{\omega^{k+1} - \omega^k}{\Delta t^k}, \tag{57}$$

where the superscript k denotes iterations and Δt^k could be increased as the solution approaches convergence. In the calculations reported here Δt^k was kept fixed. Note that once convergence is achieved, $\omega^{k+1} = \omega^k$.

In both the streamfunction–vorticity and primitive variable finite difference formulations used in this paper, an iterative line Gauss–Seidel technique was used to solve for each dependent variable. A more efficient block technique could have also been used in conjunction with the Newton–Raphson method to determine simultaneously the values of all dependent variables. Such a block method, however, was not used in the calculations presented in the next section.

Owing to the non-linear coupling between equations, underrelaxation was used in both the streamfunction–vorticity and primitive-variable finite difference formulations.

PRESENTATION OF RESULTS

Figures 4–24 show the axial velocity profiles and the electric potential profiles at different axial locations along the channel, the wall and centreline pressures along the channel, and the wall electric potential for different Reynolds numbers, interaction parameters, electrode lengths and wall conductivities. For the sake of convenience we will first discuss the results corresponding to the reference calculation defined as that corresponding to $Re=500$, $N=5$, $\phi_e=1{\cdot}5$, $\bar{\sigma}=0$ and $L_e=5$ (Figures 4–7). The results presented in Figures 8–24 will be compared in the following subsections with those of the reference case in order to determine the effects of Re, N, ϕ_e, $\bar{\sigma}$ and L_e on both the hydrodynamic and electric fields.

Reference calculations

Figures 4–7 show the profiles of axial velocity, electric potential, wall electric potential and pressure at the channel wall and at the channel centreline as a function of the axial distance along the channel. In these figures as well as those of other sections, the solid, dashed and chain lines correspond to the calculations performed with the finite element, the primitive-variable finite difference and the streamfunction–vorticity finite difference methods respectively.

The profiles shown in Figure 4 indicate that the axial velocity is distorted by the applied electric and magnetic fields before the fluid reaches the electrode entrance located at $x=-2{\cdot}50$. Far upstream and far downstream ($x=60$) the axial velocity profile is parabolic and becomes almost flat at $x=-2{\cdot}94$.

At the electrode entrance ($x=-2{\cdot}50$) the axial velocity profile exhibits two peaks: one located near the channel wall and the other located near the channel centreline. At mid-electrode, only the axial velocity peak near the channel wall can be observed. The magnitude of this axial velocity peak increases as the fluid moves along the channel and is very pronounced at $x=4{\cdot}74$. Note that the axial velocity at the channel centreline, which has a value equal to 1·5 far upstream and far downstream from the electrodes, decreases along the channel as a result of the applied electric and magnetic fields. This decrease causes the axial velocity profiles to exhibit M-shapes in the electrode region.

Figure 4 also indicates that the electromagnetic body forces decrease downstream of the electrode and that the axial velocity profiles relax from their M-shapes at $x=4{\cdot}74$ to their parabolic shapes at $x=60$. The results shown in Figure 4 indicate that the primitive-variable finite difference formulation predicts steeper axial velocity profiles at the channel wall and lower axial velocities at the channel centreline than the streamfunction–vorticity finite difference method and the finite element formulation. At $x=60$ the results presented in Figure 4 indicate that the finite difference and finite element methods yield identical axial velocity profiles.

Figure 5 shows the electric potential at selected axial locations along the channel and indicates that the electric potential is an almost linear function of the transverse co-ordinate y at a given axial location. Figure 5 also shows that there are very few differences between the results of the

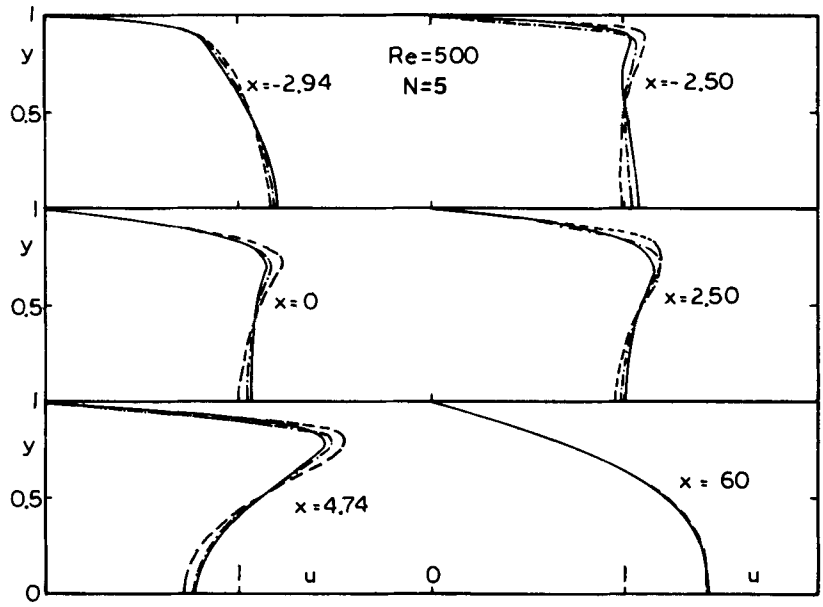

Figure. 4. Axial velocity profiles along the channel ($Re=500$, $N=5$, $\phi_e=1{\cdot}5$, $\bar{\sigma}=0$ and $L_e=5$)

finite difference and finite element methods. Note that the derivative of the electric potential with respect to y at the channel wall is zero for $|x|>2{\cdot}50$, whereas the electric potential at the wall is equal to 1·5 for $|x|\leqslant 2{\cdot}50$, i.e. in the electrode region.

Figure 6 shows the wall electric potential as a function of the axial distance along the channel. This figure indicates that the electric potential decreases quite rapidly away from the electrode edges and that the finite element method predicts slightly higher electric potential at the wall than the streamfunction–vorticity and primitive-variable finite difference formulations.

Figure 7 illustrates the fluid pressure at the channel centreline (C) and at the channel wall (W) as a function of x. The symbols I and O in Figure 7 denote the electrode entrance and exit respectively. Note that $p(-\infty, y)=0$ and therefore $\Delta p=p(x, y)-p(-\infty, y)=p(x, y)$.

In a channel flow without electromagnetic body forces, the pressure decreases linearly with the axial co-ordinate x along the channel. The results shown in Figure 7 indicate that, in the presence of electromagnetic body forces, the pressure at the wall and at the centreline increases along the channel and between the entrance and exit of the electrode. This pressure increase is caused by the Lorentz force and exhibits 'pinch' effects at the electrode entrance and exit, where the wall pressure is lower and higher respectively than the centreline pressure.

The results shown in Figure 7 indicate that the finite element method predicts slightly higher pressures at the channel wall and at the channel centreline than the finite difference formulations. The finite element method also predicts more pronounced 'pinch' effects at the electrode entrance and exit than the finite difference techniques, and the streamfunction–vorticity formulation predicts higher and lower pressures than the finite element method and the primitive-variable finite difference technique upstream and downstream of the electrodes respectively. The pressure overprediction and pressure underprediction seem to be due to the calculation of the pressure. In both the finite element method and the primitive-variable finite difference technique the pressure is directly calculated, whereas in the streamfunction–vorticity finite difference formulation the pressure is evaluated once the velocity components are calculated. The velocity components in the

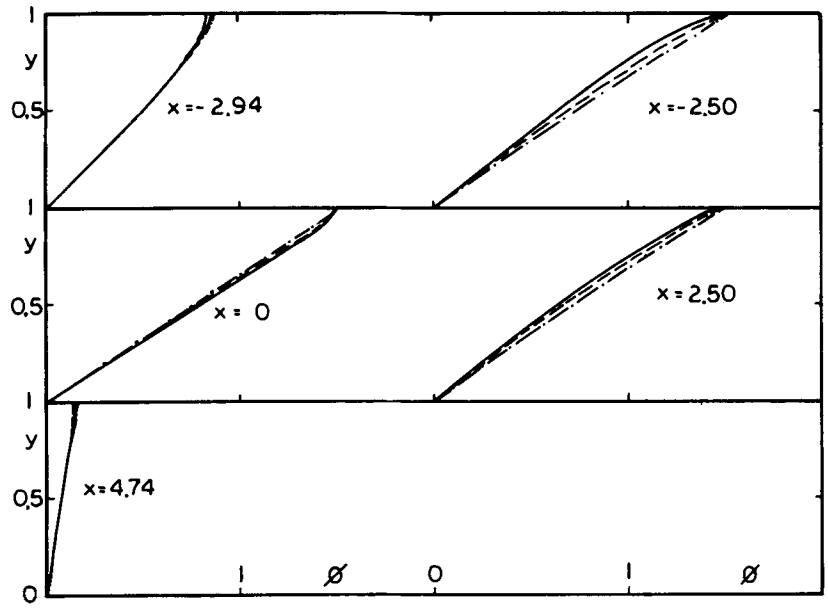

Figure 5. Electric potential profiles along the channel ($Re = 500$, $N = 5$, $\phi_e = 1{\cdot}5$, $\bar{\sigma} = 0$ and $L_e = 5$)

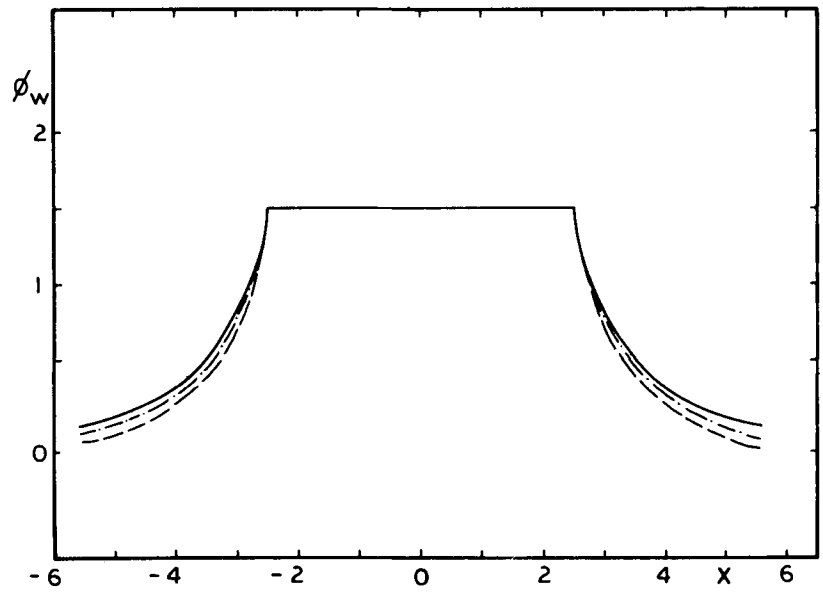

Figure 6. Wall electric potential ($Re = 500$, $N = 5$, $\phi_e = 1{\cdot}5$, $\bar{\sigma} = 0$ and $L_e = 5$)

streamfunction–vorticity formulation are obtained from the differentiation of the streamfunction (this differentiation introduces computational noise because the streamfunction is only evaluated at the grid points), and the pressure is obtained from the integration of the Navier–Stokes equations (integration is a smoothing operation which eliminates some of the computational noise introduced by the differentiation of the streamfunction).

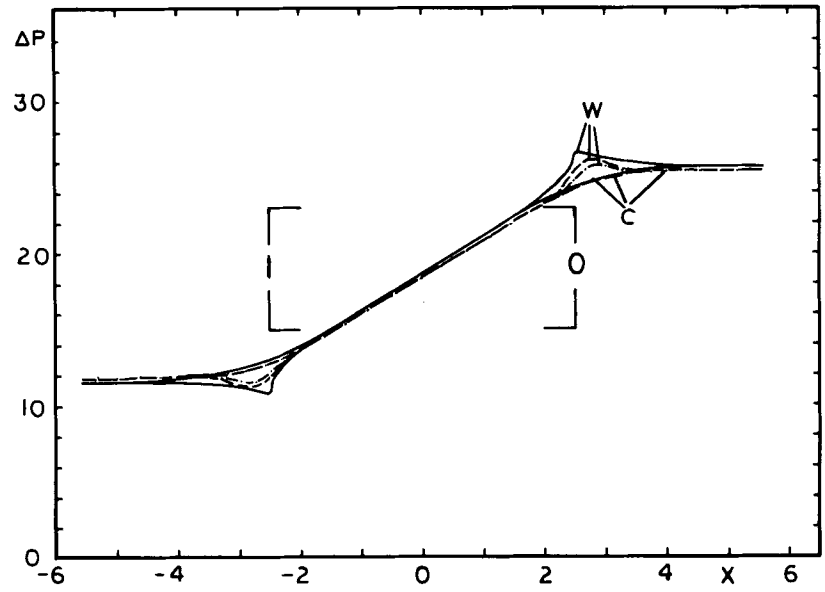

Figure 7. Pressure at the channel wall and at the channel centreline ($Re=500$, $N=5$, $\phi_e=1{\cdot}5$, $\bar{\sigma}=0$ and $L_e=5$)

Reynolds number effects

Figures 8–11 show the profiles of axial velocity, wall electric potential, electric potential and pressure at selected axial locations along the channel. The results presented in Figures 8–11 correspond to $Re=1000$, $N=5$, $\phi_e=1{\cdot}5$, $\bar{\sigma}=0$ and $L_e=5$; therefore the difference between the results presented in Figures 4–7 and 8–11 is the Reynolds number, and a comparison between these two sets of figures permits one to assess the effects of the Reynolds number on the hydrodynamic and electric fields.

A comparison between Figures 4 and 8 indicates that the characteristics of the flow field at $Re=1000$ are similar to those corresponding to $Re=500$, i.e. the parabolic velocity profile is distorted into M-shaped profiles as the fluid moves along the channel. Such a comparison also reveals that the axial velocity distortion increases as the Reynolds number is increased. In particular, the M-shaped velocity profiles are more pronounced at $x=0$, 2·5, 4·74 and 60 at $Re=1000$ than at $Re=500$. Furthermore, Figures 4 and 8 also indicate that the axial velocity profiles at $x=-2{\cdot}94$ and $-2{\cdot}50$ are almost the same at $Re=500$ and 1000; however, the axial velocity profile at $x=60$ for $Re=500$ is parabolic whereas it still exhibits an M-shape at the same location at $Re=1000$. The longer persistence of the M-shaped profiles as the Reynolds number is increased is a direct consequence of the lesser importance of viscous effects as the Reynolds number is increased.

Figures 4 and 8 also show that the differences between the finite element and finite difference formulations increase as the Reynolds number is increased, and indicate that the primitive-variable finite difference formulation predicts steeper axial velocity gradients at the channel wall and more pronounced axial velocity peaks than the finite element and streamfunction–vorticity formulations. Note that the axial velocity at the centreline decreases as the Reynolds number is increased in the electrode region.

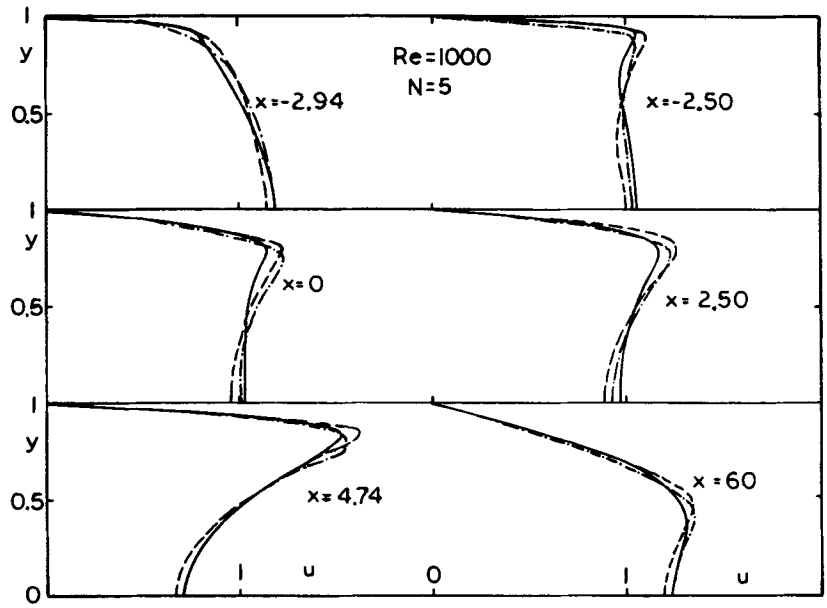

Figure 8. Axial velocity profiles along the channel ($Re = 1000$, $N = 5$, $\phi_e = 1{\cdot}5$, $\bar{\sigma} = 0$ and $L_e = 5$)

The electric potential profiles shown in Figures 5 and 9 are almost independent of the Reynolds number for the calculations performed with the finite element method; however, the primitive-variable and streamfunction–vorticity formulations predict smaller and higher electric potentials respectively than the finite element method at $Re = 1000$, whereas they predict higher electric potentials at $Re = 500$. The wall electric potentials are almost the same for $Re = 500$ and 1000 (Figures 6 and 10), and the finite element method predicts higher wall potential than the streamfunction–vorticity and primitive-variable formulations.

The pressure increase shown in Figure 11 is smaller than that of Figure 7 owing to the higher Reynolds number and the lesser importance of viscosity as the Reynolds number is increased.

Figure 11 clearly indicates that the pressure along the channel centreline is smaller than that along the channel wall for $|x| < 2{\cdot}50$. At the electrode entrance and exit, both Figures 7 and 11 show electromagnetic pinch effects whose magnitude is almost independent of the Reynolds number.

A noticeable difference between the results of Figures 7 and 11 is that the primitive-variable finite difference formulation predicts higher and lower pressure values than the finite element formulation upstream and downstream of the electrode edges respectively. The finite element method, however, predicts higher pinch effects than the finite difference techniques.

Interaction parameter effects

Figures 12–15 show the profiles of axial velocity, electric potential, wall electric potential and pressure at selected locations along the channel. These figures correspond to $Re = 1000$, $N = 10$, $\phi_e = 1{\cdot}5$, $\bar{\sigma} = 0$ and $L_e = 5$ and will be compared with Figures 8–11 in order to determine the effects of the interaction parameter on the hydrodynamic and electric fields.

Figures 8 and 12 indicate that the distortion of the axial velocity profiles increases as the interaction parameter is increased; in particular, Figure 12 indicates that the axial velocity exhibits

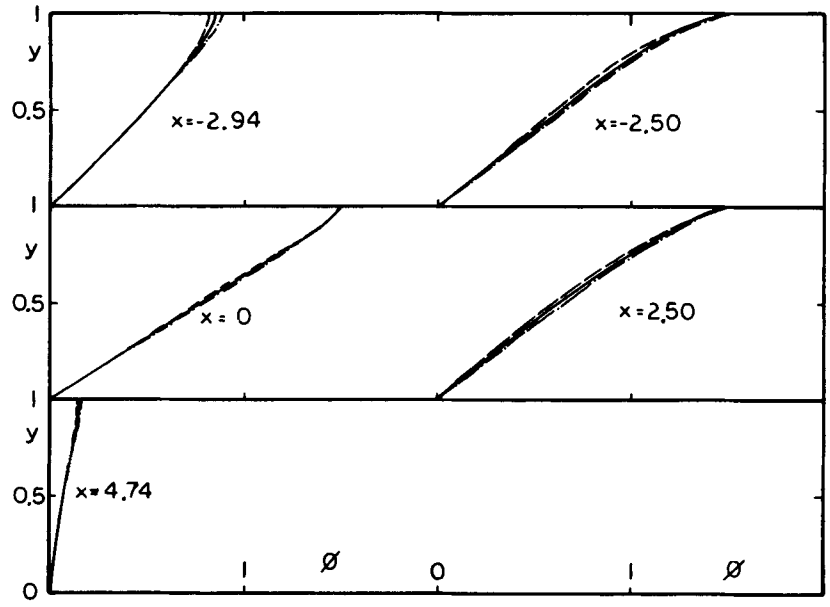

Figure 9. Electric potential profiles along the channel ($Re = 1000$, $N = 5$, $\phi_e = 1{\cdot}5$, $\bar{\sigma} = 0$ and $L_e = 5$)

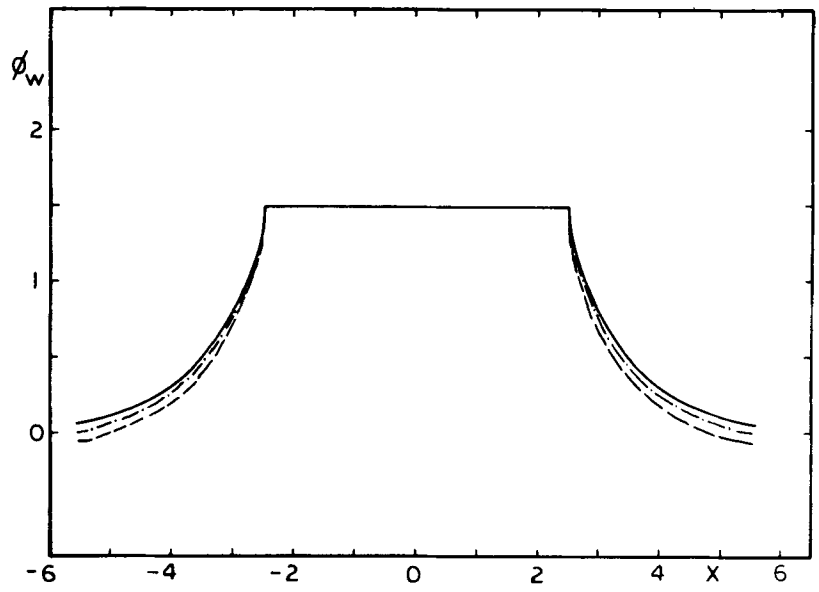

Figure 10. Wall electric potential ($Re = 1000$, $N = 5$, $\phi_e = 1{\cdot}5$, $\bar{\sigma} = 0$ and $L_e = 5$)

an M-shaped profile at $x = -2{\cdot}50$, and this M-shape becomes more pronounced as the fluid moves along the electrode region (compare Figures 8 and 12 at $x = 2{\cdot}50$ and $4{\cdot}74$). Both Figures 8 and 12 also indicate that the axial velocity relaxation distance downstream of the electrode increases as the interaction parameter is increased, i.e. the distance required for the velocity profile to reach a

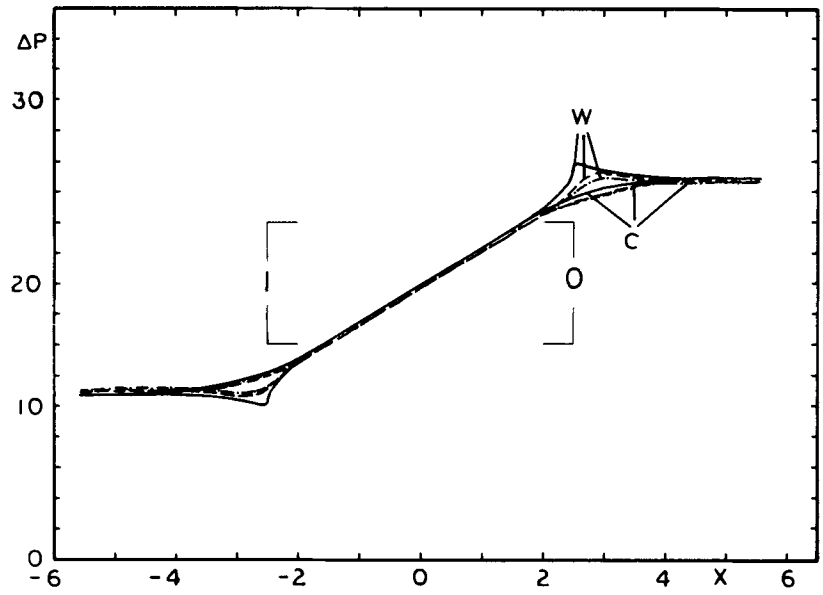

Figure 11. Pressure at the channel wall and at the channel centreline ($Re = 1000$, $N = 5$, $\phi_e = 1{\cdot}5$, $\bar{\sigma} = 0$ and $L_e = 5$)

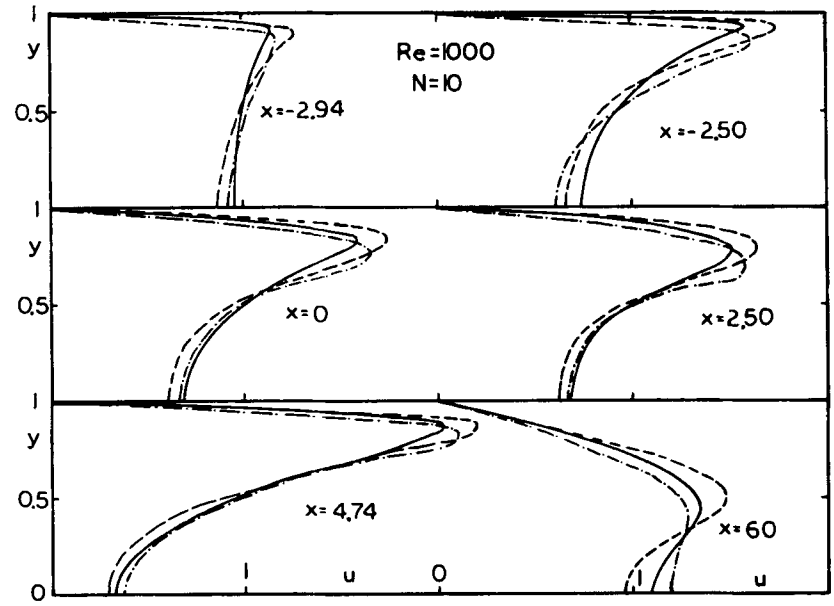

Figure 12. Axial velocity profiles along the channel ($Re = 1000$, $N = 10$, $\phi_e = 1{\cdot}5$, $\bar{\sigma} = 0$ and $L_e = 5$)

parabolic shape downstream from the electrode increases as the interaction parameter is increased.

Figures 8 and 12 also indicate that the effects of the applied electric and magnetic fields increase upstream as the interaction parameter is increased. They also indicate that the differences between

the finite difference and finite element methods increase as N is increased. In particular, the axial velocity profiles predicted by the primitive-variable finite difference method feel the effects of the applied electromagnetic field farther upstream and farther downstream than the finite element and streamfunction–vorticity formulations.

The axial velocity profiles predicted by the streamfunction–vorticity formulation relax at a faster rate than those of the finite element method and primitive-variable formulations, as indicated in Figure 12 at $x=60$.

Figures 9 and 13 indicate that the electric potential across the channel decreases as the interaction parameter is increased and that the streamfunction–vorticity formulation predicts a higher electric potential than the finite element and primitive-variable formulations; however, the finite element method predicts a higher electric potential at the channel wall than the finite difference techniques (Figure 14).

Figures 10 and 14 indicate that the wall electric potential downstream of the electrodes is almost independent of the interaction parameter; however, upstream of the electrodes, the streamfunction–vorticity and primitive-variable formulations predict higher electric potentials at the wall than the finite element method for $N=5$ than for $N=10$, whereas the results of the finite element method are almost independent of the interaction parameter.

Figures 11 and 15 indicate that the electromagnetic pinch effects at the electrode entrance and exit, the pressure increases along the electrode and the differences between the pressure at the channel wall and at the channel centreline increase as the interaction parameter is increased. Figures 11 and 15 also show that the finite element method predicts higher pressures at the channel wall and at the channel centreline and higher electromagnetic pinch effects between the electrodes than the primitive-variable and streamfunction–vorticity finite difference formulations; however, upstream and downstream of the electrodes the streamfunction–vorticity formulation predicts higher and lower Δp respectively than the primitive-variable and finite element methods.

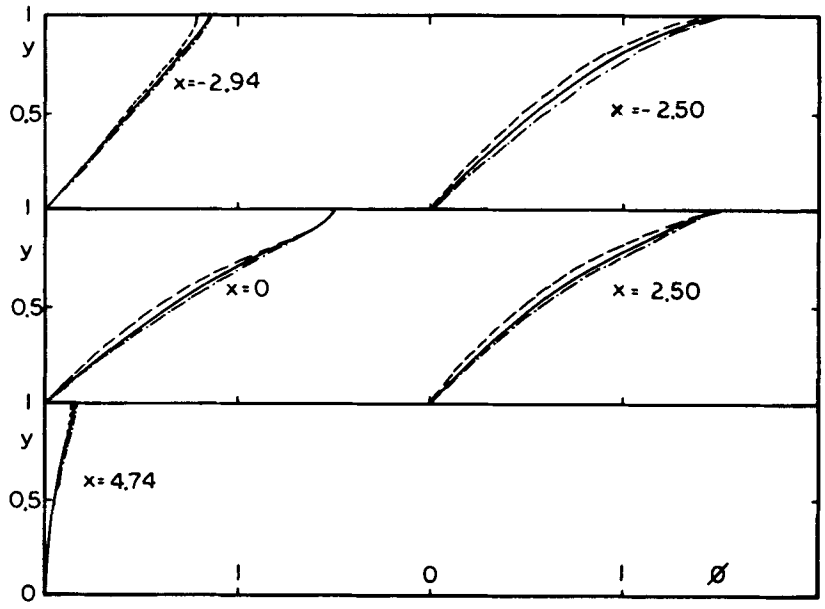

Figure 13. Electric potential profiles along the channel ($Re=1000$, $N=10$, $\phi_e=1{\cdot}5$, $\bar{\sigma}=0$ and $L_e=5$)

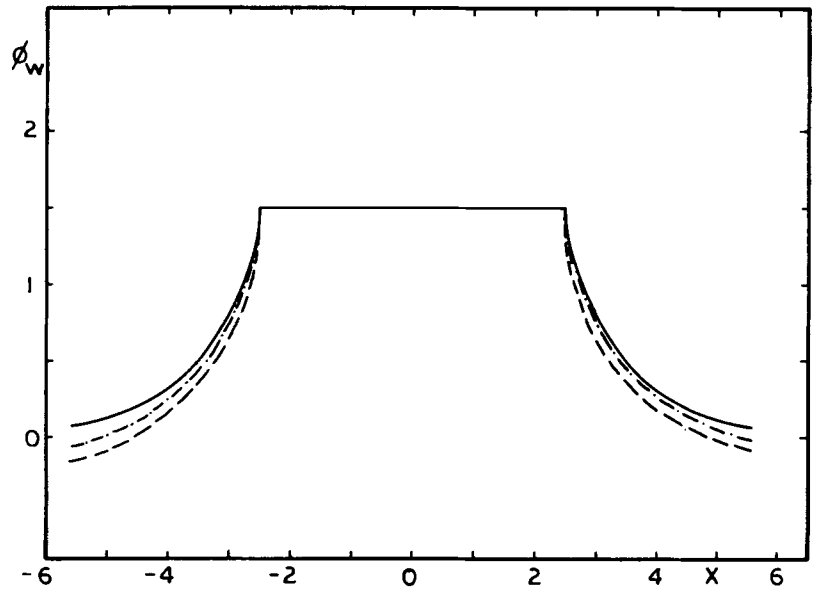

Figure 14. Wall electric potential ($Re = 1000$, $N = 10$, $\phi_e = 1{\cdot}5$, $\bar{\sigma} = 0$ and $L_e = 5$)

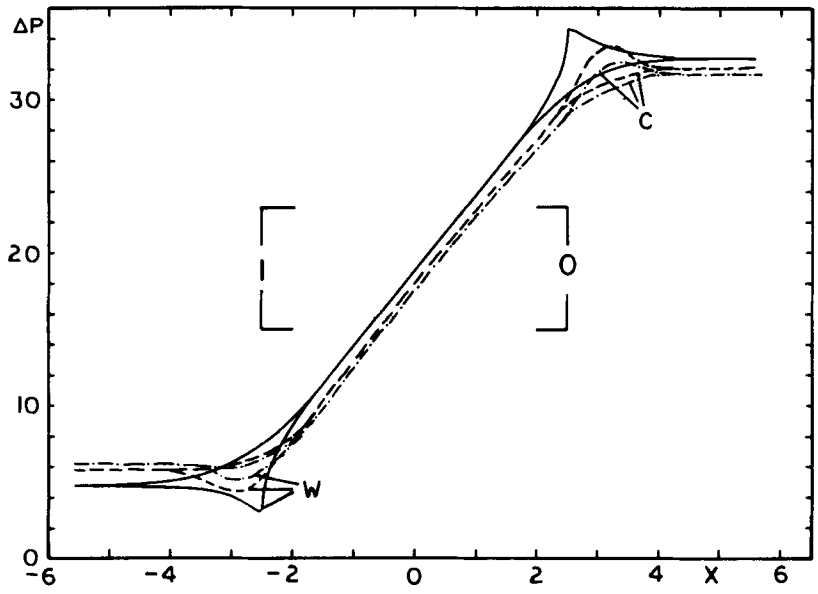

Figure 15. Pressure at the channel wall and at the channel centreline ($Re = 1000$, $N = 10$, $\phi_e = 1{\cdot}5$, $\bar{\sigma} = 0$ and $L_e = 5$)

Wall conductivity effects

Figures 16–19 show the profiles of axial velocity, electric potential, wall electric potential and pressure at the channel wall and at the channel centreline, at selected axial locations along the channel. These figures correspond to $Re = 1000$, $N = 10$, $\phi_e = 1{\cdot}5$, $\bar{\sigma} = 0{\cdot}3$ and $L_e = 5$ and will be compared with Figures 12–15 in order to assess the effects of the wall conductivity on the hydrodynamic and electric fields.

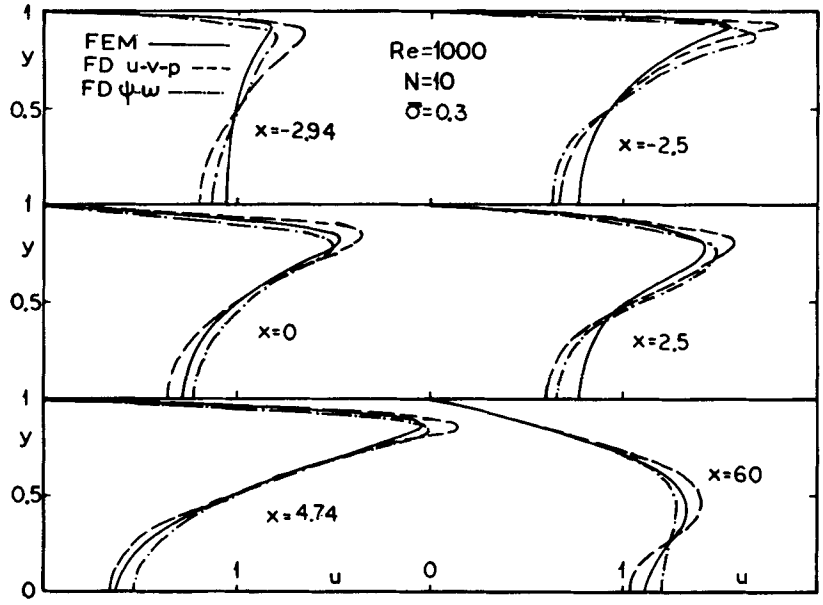

Figure 16. Axial velocity profiles along the channel ($Re = 1000$, $N = 10$, $\phi_e = 1{\cdot}5$, $\bar{\sigma} = 0{\cdot}3$ and $L_e = 5$)

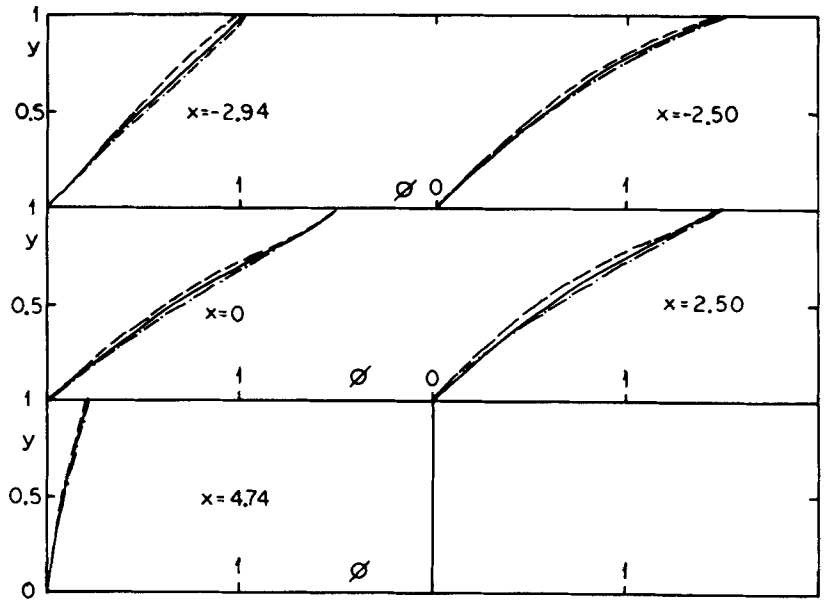

Figure 17. Electric potential profiles along the channel ($Re = 1000$, $N = 10$, $\phi_e = 1{\cdot}5$, $\bar{\sigma} = 0{\cdot}3$ and $L_e = 5$)

Figures 12 and 16 indicate that the effect of increasing the wall conductivity is to slightly decrease the peak of the M-shaped axial velocity profiles (compare Figures 12 and 16 at $x = 0$, 2·5, 4·74 and 60). The finite difference and finite element methods used in this paper predict almost the same decrease in the axial velocity profiles as $\bar{\sigma}$ is increased from 0 to 0·3. However, the magnitude of the electric potential at a given axial location increases as $\bar{\sigma}$ is increased, and the

streamfunction–vorticity formulation predicts a higher electric potential than the finite element and primitive-variable methods (compare Figures 13 and 17).

Figure 18 shows that the wall electric potential increases as $\bar{\sigma}$ is increased upstream and downstream of the electrodes. Figure 18 also shows that, for $\bar{\sigma}=0{\cdot}3$, the streamfunction–vorticity technique predicts a higher wall electric potential than the finite element and primitive-variable methods, whereas the finite element formulation predicts a higher wall potential than the streamfunction–vorticity and primitive-variable methods for $\bar{\sigma}=0$.

The differences between the results shown in Figures 12–15 and 16–19 are entirely due to the boundary conditions at the channel walls, which are electrical conductors and insulators for $\bar{\sigma}=0{\cdot}3$ and 0 respectively.

Figures 15 and 19 indicate that the pressure increase at the channel centreline and at the channel wall, and the electromagnetic pinch effect at the electrode entrance and exit, decrease as the wall conductivity is increased. Furthermore, the pinch effect is smoother for $\bar{\sigma}=0{\cdot}3$ than for $\bar{\sigma}=0$.

Figures 15 and 19 also indicate that the values of Δp predicted by the finite difference and finite element methods downstream of the electrode are almost independent of the wall conductivity, whereas the values of Δp upstream of the electrode decrease as the wall conductivity is increased. The finite element method predicts lower and higher values of Δp upstream and downstream of the electrodes respectively than the primitive-variable and streamfunction–vorticity formulations.

Electrode length effects

Figures 20–24 show the profiles of axial velocity, pressure at the channel wall and at the channel centreline, electric potential and wall electric potential as a function of the axial co-ordinate along the channel. These figures correspond to $Re=1000$, $N=10$, $\phi_e=1{\cdot}5$, $L_e=1$, $\bar{\sigma}=0$ and $\bar{\sigma}=0{\cdot}3$ and will be compared with Figures 12–15 to assess the effects of the electrode length; they will also be compared amongst themselves to determine the effects of the wall conductivity on the hydrodynamic and electric fields for $L_e=1$.

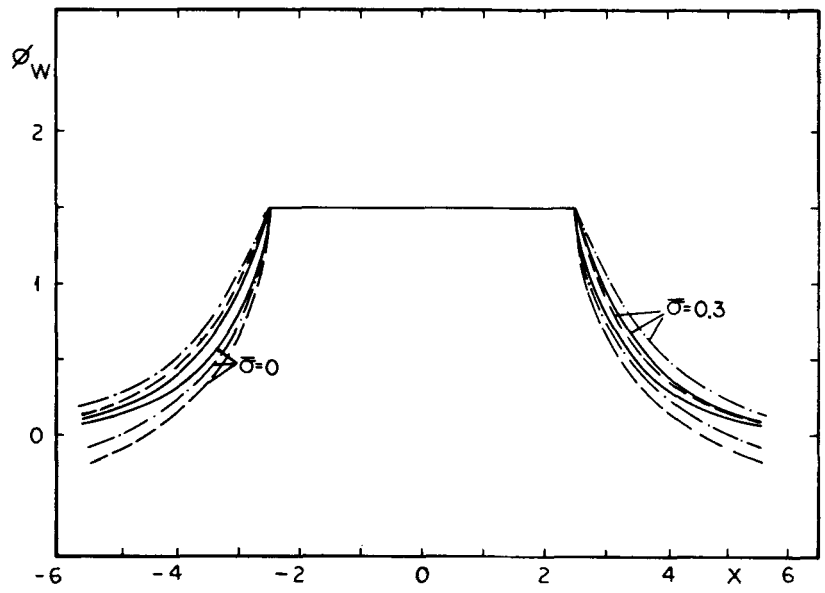

Figure 18. Wall electric potential ($Re=1000$, $N=10$, $\phi_e=1{\cdot}5$, $\bar{\sigma}=0{\cdot}3$ and $L_e=5$)

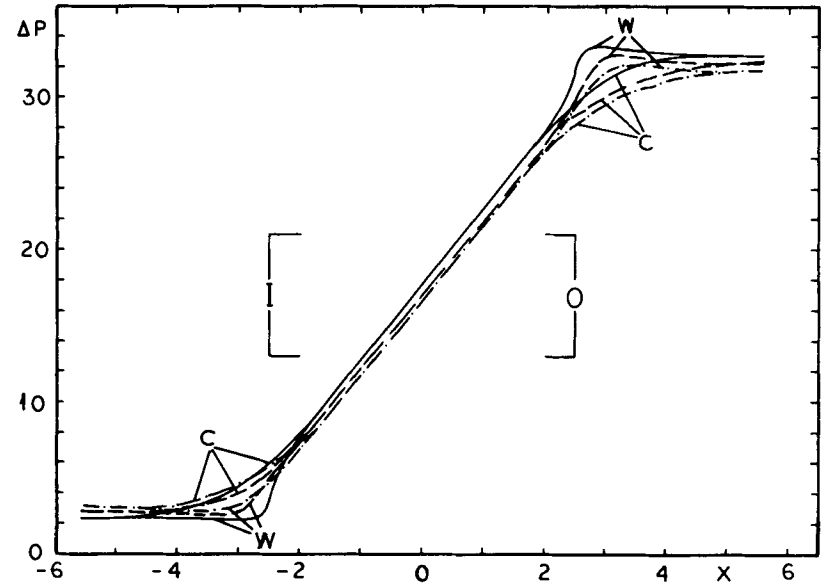

Figure 19. Pressure at the channel wall and at the channel centreline ($Re = 1000$, $N = 10$, $\phi_e = 1{\cdot}5$, $\bar{\sigma} = 0{\cdot}3$ and $L_e = 5$)

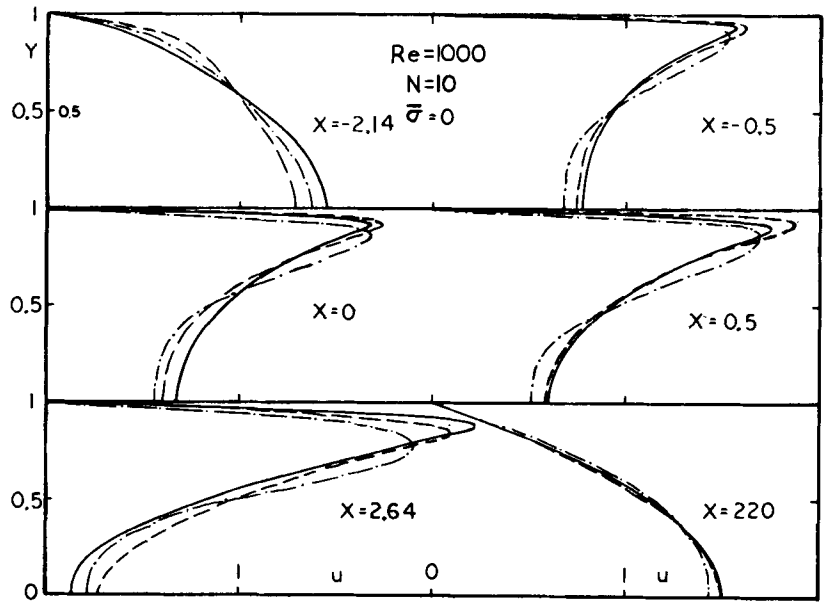

Figure 20. Axial velocity profiles along the channel ($Re = 1000$, $N = 10$, $\phi_e = 1{\cdot}5$, $\bar{\sigma} = 0$ and $L_e = 1$)

Figures 12 and 20 clearly indicate that the upstream and downstream distortion of the axial velocity profiles increases as the electrode length is increased. For example, the axial velocity profiles at $x = -2{\cdot}14$ for $L_e = 1$ exhibit an almost parabolic shape (Figure 20) whereas those corresponding to $L_e = 5$ and $x = -2{\cdot}94$ are flattened by the applied electromagnetic field (Figure

12). The M-shaped axial velocity profiles are more pronounced and the axial velocity peak is larger and closer to the channel wall for $L_e = 1$ than for $L_e = 5$ at $x = 0$.

Figure 21 shows the pressure at the channel wall and at the channel centreline, and clearly illustrates the electromagnetic pinch effect at the electrode entrance and exit. The values of Δp at the channel centreline and at the channel wall are the same at $x = 0$, i.e. at mid-electrode. The finite element method predicts a larger Δp for $x > 0$ than the primitive-variable and streamfunction–vorticity formulations, and the results of the primitive-variable finite difference scheme indicate that the values of Δp at the channel wall and at the channel centreline become equal at larger distances downstream and upstream of the electrodes than those of the streamfunction–vorticity and finite element formulations.

A comparison between Figures 15 and 21 shows that the magnitude of the electromagnetic pinch effect increases as the electrode length decreases, Δp increases as the electrode length is increased, and the finite element method predicts a higher Δp at $x = 0$ than the finite difference formulations.

Figure 22 shows the values of Δp for an electrode length $L_e = 1$ and $\bar{\sigma} = 0{\cdot}3$. A comparison between Figures 21 and 22 indicates that the electromagnetic pinch effect and the values of Δp decrease as the wall conductivity is increased. Figures 21 and 22 also show that the values of Δp corresponding to $\bar{\sigma} = 0{\cdot}3$ upstream of the electrodes are smaller than those corresponding to $\bar{\sigma} = 0$, in agreement with the results presented in Figures 12–17. The differences between Figures 21 and 22 upstream of the electrodes are entirely due to the wall conductivity.

Figure 23 shows the electric potential profiles along the channel wall for $\bar{\sigma} = 0{\cdot}3$. The electric potential corresponding to $\bar{\sigma} = 0$ is almost indistinguishable from those corresponding to $\bar{\sigma} = 0{\cdot}3$ and is not shown in Figure 23.

Figure 23 indicates that the electric potential is an almost linear function of the y-co-ordinate, with a concavity towards the channel axis caused by the hydrodynamic field. Figure 23 also

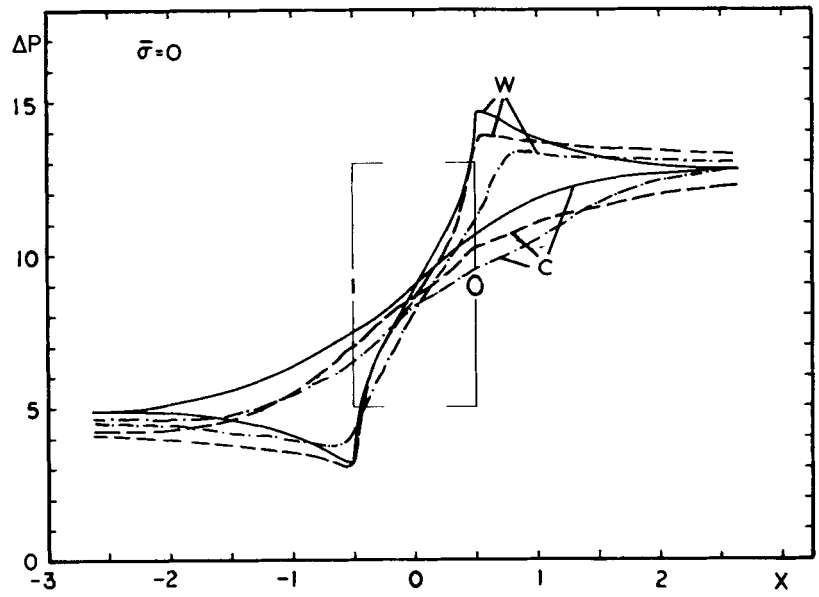

Figure 21. Pressure at the channel wall and at the channel centreline ($Re = 1000$, $N = 10$, $\phi_e = 1{\cdot}5$, $\bar{\sigma} = 0$ and $L_e = 1$)

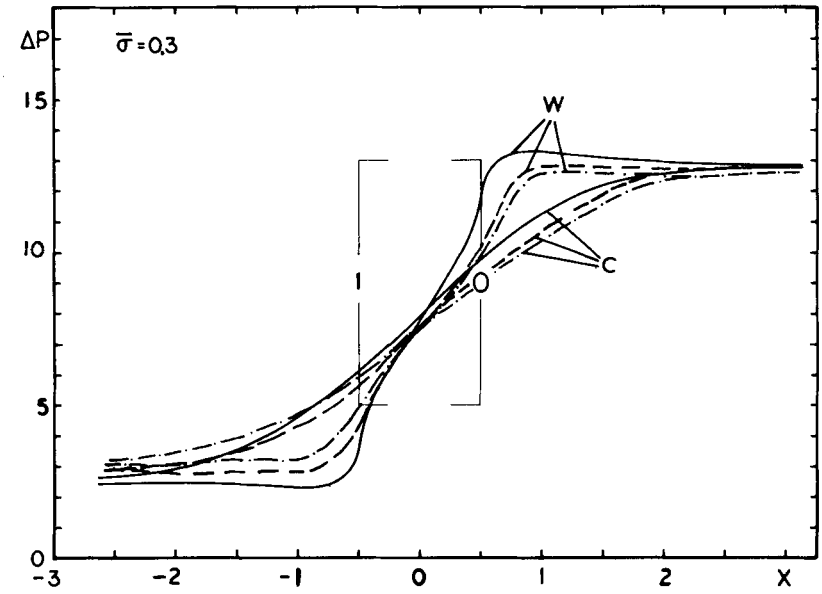

Figure 22. Pressure at the channel wall and at the channel centreline ($Re = 1000$, $N = 10$, $\phi_e = 1{\cdot}5$, $\bar{\sigma} = 0{\cdot}3$ and $L_e = 1$)

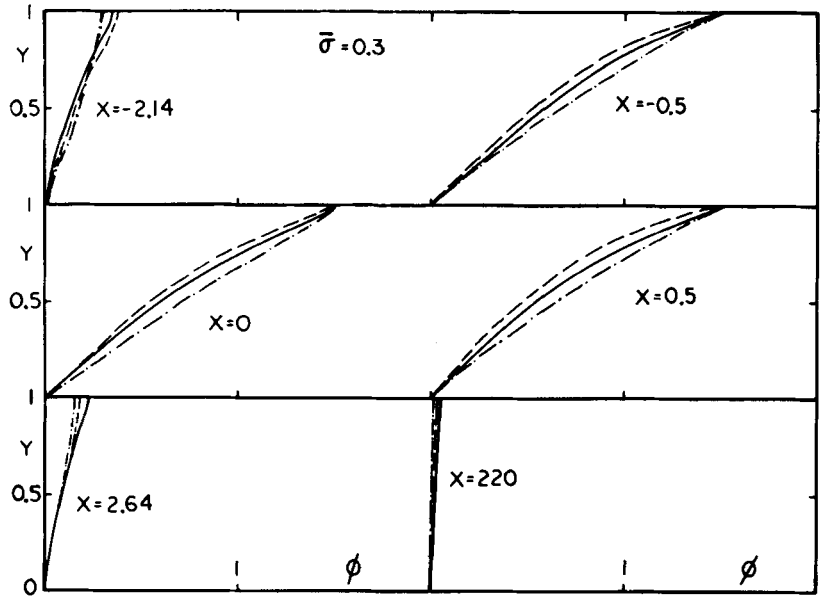

Figure 23. Electric potential profiles along the channel ($Re = 1000$, $N = 10$, $\phi_e = 1{\cdot}5$, $\bar{\sigma} = 0{\cdot}3$ and $L_e = 1$)

indicates that the electric potential at the wall rapidly decreases upstream and downstream of the electrode edges as shown in Figure 24.

Figure 24 shows the wall electric potential for an electrode of length $L_e = 1$ and $\bar{\sigma} = 0$ and 0·3, and indicates that downstream of the electrodes the finite element method predicts a higher electric potential than the streamfunction–vorticity and primitive-variable formulations for both

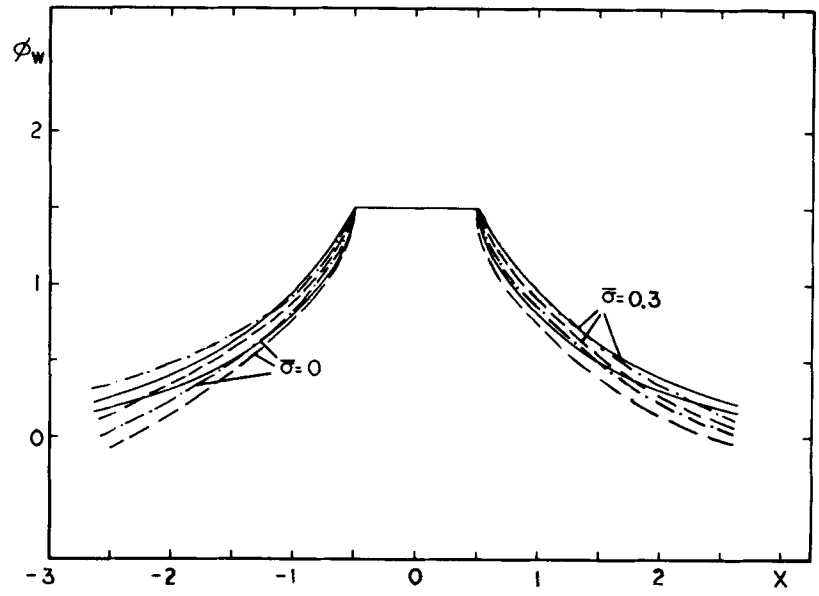

Figure 24. Wall electric potential ($Re = 1000$, $N = 10$, $\phi_e = 1{\cdot}5$, $\bar{\sigma}_1 = 0$, $\bar{\sigma} = 0{\cdot}3$ and $L_e = 1$)

$\bar{\sigma} = 0$ and 0·3. Upstream of the electrodes the streamfunction–vorticity formulation predicts a higher electric potential at the wall than the finite element and primitive-variable methods for $\bar{\sigma} = 0{\cdot}3$, whereas for $\bar{\sigma} = 0$ the electric potential at the wall predicted by the finite element method is higher than those predicted by the finite difference techniques. Both upstream and downstream of the electrodes the electric potential at the wall is higher for $\bar{\sigma} = 0{\cdot}3$ than for $\bar{\sigma} = 0$. These results are in agreement with those of Figures 12–19.

CONCLUSIONS

A Galerkin finite element method and two finite difference techniques have been used to analyse magnetohydrodynamic channel flows as a function of the Reynolds number, interaction parameter, wall conductivity and electrode length. The finite element method uses a primitive-variable formulation, bilinear interpolation for the pressure field and biquadratic interpolation functions for the velocity field and electric potential in the fluid and wall. The finite difference techniques use primitive variables and a streamfunction–vorticity formulation, and upwind/central differences for the convective terms.

The results of the calculations indicate that the applied electromagnetic field distorts the axial velocity profiles into M-shapes upstream and downstream of the electrodes. The distortion increases as the Reynolds number, interaction parameter and electrode length are increased, and decreases as the wall conductivity is increased. The results also show that the upstream influence of the applied electromagnetic field is nearly independent of the Reynolds number and that the relaxation distance of the axial velocity profiles from their M-shape in the electrode region to a parabola far away from the electrode increases as the Reynolds number is increased, owing to the lesser importance of viscous effects as that number is increased.

The axial velocity at the channel centreline decreases as the fluid moves along the electrode region and, at sufficiently high interaction parameters, recirculation zones may be created near the centreline and axial velocity spikes (jets) may occur near the channel wall, in qualitative agreement with the results of asymptotic analyses.

The MHD channel flow analysed in this paper differs from previous numerical studies in that the applied magnetic field is perpendicular to the flow direction. Furthermore, the analysis presented in this paper is valid for laminar flows at relatively low interaction parameters (O (1)), and both the convective and viscous terms have been retained in the governing equations.

The profiles of the electric potential across the channel are almost linear and show a concavity towards the channel centreline. Such a concavity is due to the hydrodynamic field.

The finite element results indicate that the electric potential profiles are almost independent of the Reynolds number. The primitive-variable and streamfunction–vorticity formulations predict smaller and higher electric potentials respectively than the finite element method at a Reynolds number of 1000, whereas they predict higher electric potentials at a Reynolds number of 500.

The wall electric potential decreases quite rapidly away from the electrode edges for both insulating and conducting walls, and the finite element method predicts slightly higher wall potentials than the streamfunction–vorticity and primitive-variable techniques.

The finite difference and finite element calculations indicate that the pressure rises along the electrode region and that there are electromagnetic pinch effects at the electrode entrance and exit. The finite element method predicts more pronounced pinch effects than the finite difference techniques. The magnitude of the pinch effect decreases as the wall conductivity is increased and increases as the electrode length is decreased.

The primitive-variable finite difference method predicts steeper axial velocity gradients at the channel wall and lower velocities at the centreline than the streamfunction–vorticity finite difference technique and the finite element formulation. These differences seem to be due to the different grids used in the calculations and the method used to evaluate the pressure. In the finite element method and in the primitive-variable finite difference method the pressure at the nodal points and a Poisson equation for the pressure respectively are solved, whereas in the streamfunction–vorticity formulation the velocity field is first obtained by differentiation of the streamfunction and then the pressure field is calculated by integration of the Navier–Stokes equations. The differentiation of the streamfunction introduces computational noise, since the streamfunction is only evaluated at the (discrete) grid points. This computational noise is smoothed out when the pressure field is calculated by integrating the linear momentum equations.

The results of the calculations also indicate that the pressure and the electromagnetic pump power increase as the Reynolds number, interaction parameter and electrode length are increased. However, the distance required for the flow to reach a fully developed, laminar profile downstream of the electrode increases as the aforementioned parameters are increased. For a Reynolds number of 1000, an interaction parameter equal to 10 and an electrode length equal to five times the channel half-width, the flow is fully developed at a distance of about 200 channel widths downstream of the electrode.

The differences between the results of the finite difference and finite element methods increase as the Reynolds number and interaction parameter are increased.

ACKNOWLEDGEMENTS

The finite difference calculations presented in this paper were performed on a CRAY X-MP and a CRAY Y-MP at the Pittsburgh Supercomputing Center, and were supported by 1988 and 1989 CRAY Research and Development Grants from CRAY Research, Inc. The authors appreciate the support provided by CRAY Research, Inc. and by the Pittsburgh Supercomputing Center.

Some of the calculations in this paper were presented at the Fifth International Conference on Numerical Methods in Laminar and Turbulent Flow held in Montreal, Canada on 6–10 July 1987 and at the Seventh International Conference on Finite Element Methods in Flow Analysis held in Huntsville, Alabama on 3–7 April 1989.

REFERENCES

1. S. T. Wu, 'Unsteady MHD duct flow by the finite element method', *Int. j. numer. methods eng.*, **6**, 3–10 (1973).
2. B. Singh and J. Lal, 'Finite element method in magnetohydrodynamic channel flow problems', *Int. j. numer. methods eng.*, **15**, 1104–1111 (1982).
3. B. Singh and J. Lal, 'Effect of magnetic field orientation and wall conductivity on MHD channel flows using finite element method', *Comput. Methods Appl. Mech. Eng.*, **40**, 159–170 (1983).
4. Yu. M. Gel'fgat, D. E. Peterson and E. V. Shcherbinin, 'Velocity structure of flows in nonuniform magnetic fields: Part 1. Numerical calculations', *Magnetohydrodynamics*, **14**(1), 55–61 (1978).
5. G. Yagawa and M. Masuda, 'Finite element analysis of magnetohydrodynamics and its application to lithium blanket design of a fusion reactor', *Nucl. Eng. Design*, **71**, 121–136 (1982).
6. N. S. Winowich and W. F. Hughes, 'A finite-element analysis of two-dimensional MHD flow', in H. Branover, A. Yakhot and P. S. Lykoudis (eds), *Liquid-Metal Flows and Magnetohydrodynamics, Progress in Astronautics and Aeronautics, Vol. 84*, AIAA, New York, 1983, pp. 313–332.
7. J. I. Ramos and N. S. Winowich, 'Magnetohydrodynamic channel flow study', *Phys. Fluids*, **29**(4), 992–997 (1988).
8. N. S. Winowich, W. F. Hughes and J. I. Ramos, 'Numerical simulation of electromagnetic pump flow', in C. Taylor, W. G. Habashi and M. M. Hafez (eds), *Numerical Methods in Laminar and Turbulent Flow, Vol. 5, Part 2*, Pineridge Press, Swansea, 1987, pp. 1228–1240.
9. N. S. Winowich, 'Magnetohydrodynamic channel flow with a nonuniform magnetic field and conductive walls', *Ph.D. Thesis*, Department of Mechanical Engineering, Carnegie-Mellon University, Pittsburgh, PA, October 1986.
10. N. S. Winowich and J. I. Ramos, 'Finite difference and finite element methods for MHD channel flows', in T. J. Chung and G. R. Karr (eds), *Finite Element Analysis in Fluids*, UAH Press, The University of Alabama in Huntsville, Huntsville, AL, 1989, pp. 934–939.
11. J. C. R. Hunt, 'Magnetohydrodynamic flow in rectangular ducts', *J. Fluid Mech.*, **21**, 577–590 (1965).
12. J. C. R. Hunt and K. Stewartson, 'Magnetohydrodynamic flow in rectangular ducts. II', *J. Fluid Mech.*, **23**, 563–581 (1965).
13. J. C. R. Hunt and S. Leibovich, 'Magnetohydrodynamic flow in channels of variable cross-section with strong transverse magnetic fields', *J. Fluid Mech.*, **28**, 241–260 (1967).
14. J. C. R. Hunt and J. A. Shercliff, 'Magnetohydrodynamics at high Hartmann number', *Ann. Rev. Fluid Mech.*, **3**, 37–62 (1971).
15. J. C. R. Hunt and G. S. S. Ludford, 'Three-dimensional MHD duct flows with strong transverse magnetic fields. Part 1. Obstacles in a constant area channel', *J. Fluid Mech.*, **33**, 693–714 (1968).
16. J. S. Walker, G. S. S. Ludford and J. C. R. Hunt, 'Three-dimensional MHD duct flows with strong transverse magnetic fields. Part 2. Variable-area rectangular ducts with conducting sides', *J. Fluid Mech.*, **46**, 657–684 (1971).
17. J. S. Walker, G. S. S. Ludford and J. C. R. Hunt, 'Three-dimensional MHD duct flows with strong transverse magnetic fields. Part 3. Variable-area rectangular ducts with insulating walls', *J. Fluid Mech.*, **56**, 121–141 (1972).
18. J. S. Walker and G. S. S. Ludford, 'Three-dimensional MHD duct flows with strong transverse magnetic fields. Part 4. Fully insulated, variable-area rectangular ducts with small divergences', *J. Fluid Mech.*, **56**, 481–496 (1972).
19. R. J. Holroyd and J. S. Walker, 'A theoretical study of the effects of wall conductivity, non-uniform magnetic fields and variable-area ducts on liquid metal flows at high Hartmann number', *J. Fluid Mech.*, **84**, 471–495 (1978).
20. B. M. Irons, 'A Frontal solution program for finite element analysis', *Int. j. numer. methods eng.*, **2**, 5–32 (1970).
21. S. V. Patankar, *Numerical Heat Transfer and Fluid Flow*, Hemisphere, Washington DC, 1980.
22. D. A. Anderson, J. C. Tannehill and R. H. Pletcher, *Computational Fluid Mechanics and Heat Transfer*, Hemisphere, Washington DC, 1984.
23. P. J. Roache, *Computational Fluid Dynamics*, Hermosa, Albuquerque, NM, 1972, p. 141.